Three new VHS-DES Quasars at $6.7 \lesssim z \lesssim 6.9$ and Emission Line Properties at $z > 6.5$

S. L. Reed[1,2,3⋆], M. Banerji[2,3], G. D. Becker[4], P. C. Hewett[2], P. Martini[5,6], R. G. McMahon[2,3], E. Pons[2], M. Rauch[7], T. M. C. Abbott[8], S. Allam[9], J. Annis[9], S. Avila[10], E. Bertin[11,12], D. Brooks[13], E. Buckley-Geer[9], A. Carnero Rosell[14,15], M. Carrasco Kind[16,17], J. Carretero[18], F. J. Castander[19,20], C. E. Cunha[21], C. B. D'Andrea[22], L. N. da Costa[15,23], J. De Vicente[14], S. Desai[24], H. T. Diehl[9], P. Doel[13], A. E. Evrard[25,26], B. Flaugher[9], J. Frieman[9,27], J. García-Bellido[28], E. Gaztanaga[19,28], D. Gruen[21,29,30], J. Gschwend[15,23], G. Gutierrez[9], D. L. Hollowood[31], K. Honscheid[5,32], B. Hoyle[33,34], D. J. James[35], K. Kuehn[36], O. Lahav[13], M. Lima[37,15], M. A. G. Maia[15,23], J. L. Marshall[38], R. Miquel[39,18], R. L. C. Ogando[15,23], A. A. Plazas[1,40], A. Roodman[21,30], E. Sanchez[14], V. Scarpine[9], M. Schubnell[26], S. Serrano[19,20], I. Sevilla-Noarbe[14], M. Smith[41], R. C. Smith[8], F. Sobreira[42,15], E. Suchyta[43], M. E. C. Swanson[17], G. Tarle[26], D. Thomas[10], D. L. Tucker[9], V. Vikram[44]
Affliations at end of paper.

23 January 2019

ABSTRACT

We report the results from a search for $z > 6.5$ quasars using the Dark Energy Survey (DES) Year 3 dataset combined with the VISTA Hemisphere Survey (VHS) and *WISE* All-Sky Survey. Our photometric selection method is shown to be highly efficient in identifying clean samples of high-redshift quasars leading to spectroscopic confirmation of three new quasars - VDESJ 0244−5008 ($z = 6.724$), VDESJ 0020−3653 ($z = 6.834$) and VDESJ 0246−5219 ($z = 6.90$) - which were selected as the highest priority candidates in the survey data without any need for additional follow-up observations. The new quasars span the full range in luminosity covered by other $z > 6.5$ quasar samples ($J_{AB} = 20.2$ to 21.3; $M_{1450} = −25.6$ to $−26.6$). We have obtained spectroscopic observations in the near infrared for VDESJ 0244−5008 and VDESJ 0020−3653 as well as our previously identified quasar, VDESJ 0224−4711 at $z = 6.50$ from Reed et al. (2017). We use the near infrared spectra to derive virial black-hole masses from the full-width-half-maximum of the MgII line. These black-hole masses are $\simeq 1 - 2 \times 10^9 M_\odot$. Combining with the bolometric luminosities of these quasars of $L_{bol} \simeq 1 - 3 \times 10^{47}$ implies that the Eddington ratios are high - $\simeq 0.6$-1.1. We consider the CIV emission line properties of the sample and demonstrate that our high-redshift quasars do not have unusual CIV line properties when compared to carefully matched low-redshift samples. Our new DES+VHS $z > 6.5$ quasars now add to the growing census of luminous, rapidly accreting supermassive black-holes seen well into the epoch of reionisation.

Key words: dark ages, reionisation, first stars — galaxies: active — galaxies: formation — galaxies: high redshift – quasars individual:

1 INTRODUCTION

The Epoch of Reionisation (EoR) represents a transformational period in the history of the Universe when it transitioned from a predominantly neutral to a predominantly ionised state. Luminous

quasars are among the best probes of this era in the Universe's history, and high signal-to-noise ratio (S/N), high-resolution spectra of the most luminous quasars can be used to determine the neutral hydrogen fraction e.g. by studying the properties of the Lyα forest and the sizes of quasar proximity zones (e.g. Fan et al. 2006; Bolton & Haehnelt 2007). Furthermore, the identification of such luminous quasars early in the Universe's history poses significant

⋆ E-mail: sophiereed@princeton.edu

challenges for theories of black-hole seed formation and growth (e.g. Volonteri 2010; Latif et al. 2013) requiring massive seeds as well as extended periods of Eddington-limited or super Eddington growth to explain the population (e.g. Sijacki et al. 2009).

Around 100 luminous quasars are now known at $z \sim 6 - 6.5$ (e.g. Bañados et al. 2016; Jiang et al. 2016; Reed et al. 2017; Wang et al. 2017). The search for luminous quasars is now being pushed to even higher redshifts, aided by the incorporation of red-sensitive CCDs and filters in wide-field "optical" surveys such as The Dark Energy Survey (DES), DECals, Pan-STARRS and Hy-perSuprimeCam (HSC). These improvements in area, depth and sensitivity enable quasars to be identified at $z > 6.5$. The challenge of identifying quasars at these highest redshifts is demonstrated clearly by the fact that for the last seven years only a single quasar was known above $z = 7$ (Mortlock et al. 2011) with the redshift record only recently broken by the $z = 7.54$ quasar identified by Bañados et al. (2018). Identifying these most distant quasars requires the combination of wide-field optical surveys (in which the quasars appear as drop-outs) with sensitive near infra-red surveys (in which the quasars are detected). Near infrared surveys such as the UKIDSS (Mortlock et al. 2011; Bañados et al. 2018), VISTA Hemisphere Survey (VHS; Venemans et al. 2015b; Pons et al. 2018) and VIKING (Venemans et al. 2013) have therefore been crucial to pushing the redshift frontiers for quasar discovery. Many of the discoveries of $z > 6.5$ quasars have come within the last year with the new data from surveys such as DES, DECals and HSC in combination with near infra-red data from UKIDSS, VHS and *WISE* playing a crucial part (Matsuoka et al. 2018b,a; Bañados et al. 2018; Wang et al. 2018; Yang et al. 2018). Identifying more quasars at these highest redshifts is critical in order to constrain models of reionisation as well as black-hole formation and growth.

In this paper we present our search for quasars with $z > 6.5$, exploiting the wide wavelength coverage provided by combining data from DES, VHS and the *WISE* All-Sky Survey. We also present new near infrared spectra for three of our four $z > 6.5$ quasars. The near infra-red spectra give us access to a whole host of rest-frame UV emission lines, which trace the dynamics of the quasar broad-line region (BLR). We use these emission lines to derive more robust redshifts, estimate black-hole masses as well as look for evidence for powerful disk winds affecting the BLR.

Throughout this paper we assume a flat ΛCDM cosmology with $\Omega_{\mathrm{M}} = 0.3$, $\Omega_{\Lambda} = 0.70$ and $H_0 = 70.0$ km s^{-1} Mpc^{-1}. All magnitudes are on the AB system, which is the native photometric system for DES. For VHS and *WISE* we have used Vega to AB conversions of $J_{\mathrm{AB}} = J_{\mathrm{Vega}} + 0.937$, $K_{\mathrm{S,AB}} = K_{\mathrm{S,Vega}} + 1.839$, $W1_{\mathrm{AB}} = W1_{\mathrm{Vega}} + 2.699$ and $W2_{\mathrm{AB}} = W2_{\mathrm{Vega}} + 3.339$[1].

2 PHOTOMETRIC SELECTION

2.1 Dark Energy Survey (DES)

In Reed et al. (2017) (R17 hereafter) we presented the discovery of eight $z > 6$ quasars identified using data from the first year of DES observations (Y1). The 10σ depths for DES Y1 from Reed et al. (2017) are $g = 24.2$, $r = 23.9$, $i = 23.3$, $z = 22.5$ and $Y = 21.2$. In this paper we use the internal DES releases (known as Y1 and Y3) corresponding to the first three years of DES observations. The DES Y3 release has been published as DES Data Release 1 (Abbott

---

Table 1. Summary of the steps in the z > 6.5 quasar candidate photometric selection process.

Step	Description	Number Removed	Number Remaining
1	Number of objects in catalogue		425,880,019
	Flag criteria		
	$Y_{\mathrm{PSF}} \leqslant 21.5$ and $\sigma_{\mathrm{Y}} < 0.2$		
	$z_{\mathrm{PSF}} - Y_{\mathrm{PSF}} > 0.5$		
	g_{PSF} and $r_{\mathrm{PSF}} > 23.0$		
	σ_g and $\sigma_r > 0.1$		
2	Match to un*WISE* forced photometry		821,709
3	$Y - J < 1.0$	606,347	215,362
4	$Y < 21.0$	171,369	43,993
5	$6.3 < z_{\mathrm{predicted}} < 7.2$	41,633	2,360
6	$\chi^2_{\mathrm{Quasar}} < 25.0$ and $\chi^2_{\mathrm{BD}} > 2.0$	2,081	279

et al. 2018) and covers $\sim$5000 deg^2 of the sky to 10σ depths of $g = 24.3$, $r = 24.1$, $i = 23.4$, $z = 22.7$ and $Y = 21.4$ in a 1.95 arcsecond diameter aperture. Thus the Y3 release probes $\sim$0.2 mags deeper than the Y1 data in the z-band and covers almost three times the area of DES Y1. We use the catalogues produced by the DES Collaboration throughout the paper. All DES magnitudes used in the paper are PSF magnitudes unless otherwise stated.

2.2 VISTA Hemisphere Survey (VHS)

The search for quasars at the highest redshifts requires the optical data from DES to be supplemented with near infrared photometry. In particular, observations in the near infra-red J-band are important to break the degeneracy in colours between cool stars and high redshift quasars at $6.6 < z < 6.8$. We therefore also make use of photometry in the J and K_S bands from the VISTA Hemisphere Survey (VHS; McMahon et al. 2013; Banerji et al. 2015) in this work. The VHS data used here covers $\sim$68% of the $\sim$5000 deg^2 area of the DES Y3 data release, discussed in Section 2.1. Thus the combined DES+VHS area within which we search for high-redshift quasars is $\sim$3400 deg^2. In this paper we make use of the VHS catalogue magnitudes measured in a two arcsec diameter aperture (*apermag3*) with an appropriate aperture correction for point sources.

2.3 WISE All-Sky Survey

Longer wavelength data at 3.4 and 4.6μm (known as the W1 and W2 bands respectively) were used from the all-sky Wide Infrared Survey Explorer dataset (*WISE*; Wright et al. 2010). We used the un*WISE* reduction of the NEOWISE-R3 images (Meisner et al. 2017). These coadd images are deeper than those in the All*WISE* data release with 5σ point source depths of $W1_{\mathrm{AB}} = 20.2$ and $W2_{\mathrm{AB}} = 19.8$. The *WISE* data overlaps with the full DES+VHS area of our search and *WISE* fluxes were measured by performing forced aperture photometry on the un*WISE* coadds using the locations of sources from the VHS J-band catalogues.

2.4 Quasar Candidate Selection via SED-fitting

In order to select high-redshift quasar candidates, a series of loose flux limits and colour cuts were first applied to the combined pho-
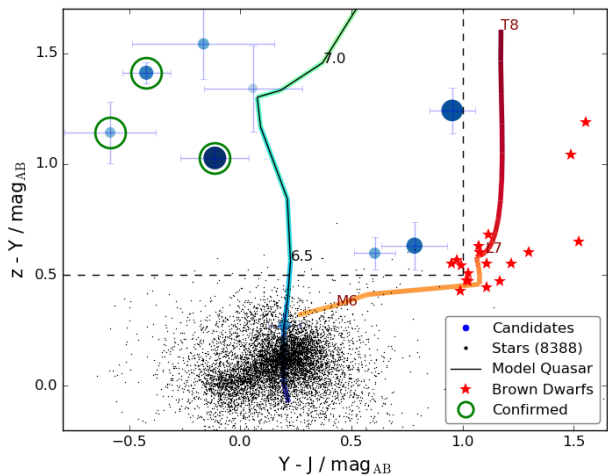
Figure 1. The initial colour selection used in this paper. The yellow-red line shows the predicted path of brown dwarfs from the models used in this paper, the red stars show the colours of known brown dwarfs taken from Kirkpatrick et al. (2011) and are mostly found outside the quasar selection box which is delineated by the dashed lines. The blue-green line shows the predicted path of quasars. The blue points show the final eight quasar candidates selected after visual inspection and the size of the points is proportional to how good their fit to a quasar model is with the largest points having the best fit. The circled objects were spectroscopically followed up and confirmed to be quasars. The small black points are a sub-sample of the DES+VHS photometric sources shown for comparison to the location of the quasar candidates.

tometric catalogues from DES + VHS + un*WISE* covering ∼3400 deg². These cuts are summarised in Table 1 in the order in which they are applied to the data. The loose colour-cuts allow us to reject sources with unphysical colours and narrow down the number of objects on which we perform full spectral energy distribution (SED) fitting. The cuts applied are broadly similar to those in R17. In that work we demonstrated that some of the high-redshift quasars recovered by our SED-fitting selection method spanned a wider range of colours compared to previous high-redshift quasar searches - e.g. VDES J2250-5015 in R17 is too red in terms of its $(Y - J)$ colour to satisfy the selections in e.g. Bañados et al. (2016) and Venemans et al. (2015a). To allow the inclusion of redder quasars in our sample we relaxed the $(Y - J)$ colour cut further from <0.8 used in R17 to <1.0 in this work. The initial colour selection box is shown in Figure 1 along with the predicted tracks of quasars and brown dwarfs and our final sample of photometric candidates that satisfy all the selection criteria.

The loose colour cuts and flux-limits result in a sample of 215,362 photometric candidates. These are further cut down to 43,993 by applying a brighter Y-band flux limit to the sample given that most optical spectrographs used for spectroscopic follow-up have relatively poor response in this wavelength range. The SED-fitting method introduced in R17 was then applied to the photometric candidates in order to estimate the probabilities of the candidate being either a quasar or a brown-dwarf. In the case of the quasar model-fits, best-fit photometric redshifts and extinctions were also derived for each candidate. The quasar and brown-dwarf models employed were identical to those in R17 (Maddox & Hewett 2006; Maddox et al. 2012; Skrzypek et al. 2015). An example of the results of SED-fitting for one of our quasar candidates, VDESJ0244-

5008 can be seen in Fig. 2. As the objective of this study was to identify quasars at the highest redshifts we selected candidates with a photometric redshift of > 6.3. This study is aimed at finding quasars with $z > 6.5$ but a slightly lower photometric redshift limit was used to allow for scatter in the photometric redshift estimate. Spectroscopic confirmation of our high-redshift quasar candidates makes use of optical spectrographs (see Section 3). We therefore also imposed an upper redshift limit of $z < 7.2$, above which the Lyα emission line redshifts out of the range of most optical spectrographs. The candidates within this redshift range were then narrowed down based on their χ^2_{Quasar} and χ^2_{BD} values, which represent the reduced χ^2 values obtained from the quasar and brown-dwarf model fits respectively. Specifically, candidates with $\chi^2_{Quasar} > 25.0$ or $\chi^2_{BD} < 2$ were removed from the sample based on the distribution of values shown in Fig. 3. This led to 279 high-redshift quasar candidates. All 279 candidates were visually inspected following which we identified eight candidates as the most probable high-redshift quasars. The colours of these eight candidates are shown in Fig. 1. During the visual inspection stage, the majority of objects removed corresponded to instances of blended sources in the un*WISE* coadds, which were resolved in the DES and VHS images. As the un*WISE* forced photometry for these blended objects was biased artifically bright, it improved their fit to a quasar model. Other sources removed include diffraction spikes, cosmic rays and saturated objects. Of the eight remaining candidates, one (VDESJ0244-5008) had already been identified by us as a high-redshift quasar candidate using DES Y1 data and was spectroscopically followed up in January 2015 (Section 3.1.3). Of the remaining seven candidates, five were detected in more than one VHS band and were therefore deemed higher priority. Two of the five candidates (VDESJ0020-3653 and VDESJ0246-5219) were visible during our spectroscopic observing runs (Section 3) and were therefore followed-up. No spectroscopy has as yet been obtained for the other candidates. DES cutout images for all three high-redshift quasars with spectroscopic follow-up observations can be seen in Fig. 4 and the photometry for all three sources is summarised in Table 2. For completeness we also include in Table 2 the properties of VDESJ0224-4711, which is the other $z \geqslant 6.5$ quasar previously identified by us using DES+VHS in R17.

3 SPECTROSCOPIC OBSERVATIONS

This section presents details of the spectroscopic observations conducted for our three $z > 6.5$ quasar candidates identified in Section 2.4. We begin by describing the optical spectroscopic observations used to confirm that our photometric candidates are true high-redshift quasars. We then present near infra-red spectra that allow us to derive emission line properties and black-hole masses for these quasars. In addition to the three $z > 6.5$ quasar candidates, we also present here new optical and near infra-red spectra for the $z = 6.50$ quasar VDESJ0244-4711, which was first identified in R17.

3.1 Optical Spectroscopy

3.1.1 Las Campanas Clay MagE

VDESJ0244-5008 was our first $z > 6.5$ quasar candidate identified using DES Y1 photometry. In January 2015 the source was observed using the Magellan Echellette (MagE) Spectrograph on the 6.5m Clay Telescope at Las Campanas. Details of the observational setup can be found in Table 3. The data were reduced using
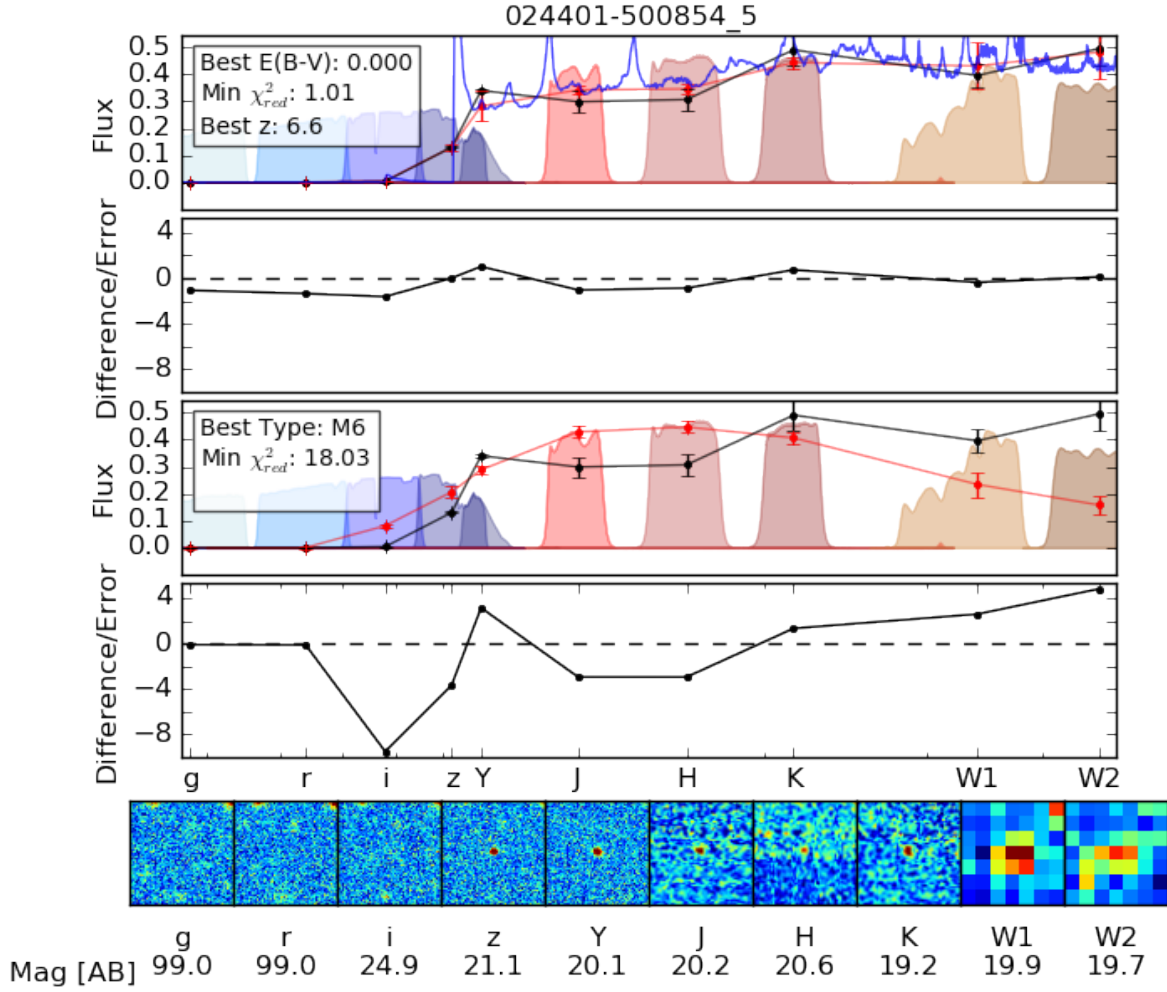
Figure 2. The SED fitting method illustrated for VDES J0244-5008 the first z > 6.5 candidate identified from DES data. The top two panels show the best quasar fit and the difference (between the predicted and actual values) divided by the total error (model error and actual error combined) for this fit respectively. The next two panels show the same for the best fitting brown dwarf model. The bottom row of images shows 20 arcsecond cutout images across the DES, VHS and *WISE* bands. VDES J0244-5008 was confirmed as a quasar with z = 6.724.

Table 2. Positions and magnitudes of the three new z > 6.5 quasars discovered in this work as well as the $z \sim 6.5$ quasar VDESJ0224-4711 from R17. The g, r and i band magnitudes are given as a 5σ magnitude limits for a 2 arcsecond aperture.

	VDES0224-4711	VDES J0244-5008	VDES J0020-3653	VDES J0246-5219
DES Tilename	DES0222-4706	DES0245-4957	DES0021-3706	DES0246-5205
RA (J2000)	36.11057	41.00424	5.13113	41.73289
	$02^h24^m26.54^s$	$02^h44^m01.02^s$	$00^h20^m31.47^s$	$02^h46^m55.89^s$
Dec. (J2000)	-47.19149	-50.14826	-36.89495	-52.33054
	-47°11'29.4"	-50°08'53.7"	-36°53'41.8"	-52°19'49.9"
g	> 25.0	> 24.0	> 24.0	> 24.0
r	> 25.0	> 24.4	25.53 ± 0.60	> 24.4
i	24.0 ± 0.4	> 23.9	25.01 ± 0.64	> 23.9
z	20.20 ± 0.02	21.08 ± 0.08	21.39 ± 0.04	21.85 ± 0.11
Y	19.89 ± 0.05	20.15 ± 0.05	19.98 ± 0.03	20.70 ± 0.08
J	19.75 ± 0.06	20.21 ± 0.15	20.40 ± 0.10	21.29 ± 0.19
Ks	18.99 ± 0.06	19.67 ± 0.14	19.55 ± 0.13	20.35 ± 0.21
W1	18.75 ± 0.05	19.91 ± 0.12	19.82 ± 0.14	20.09 ± 0.14
W2	18.6 ± 0.1	19.02 ± 0.15	19.71 ± 0.32	21.89 ± 0.81

Table 3. Observational details for the optical spectroscopy of the three new z > 6.5 quasars as well as the $z = 6.50$ quasar VDESJ0224-4711 from R17.

Name	Telescope	Instrument	Exposure Time (Seconds)	Date	Filter	Grating/ Grism
VDES J0224-4711	Gemini-S	GMOS	$300 \times 4 = 1200$	07/10/2016	RG610_G0331	R400+_G5325
VDES J0244-5008	Clay	MagE	$600 + 1200 \times 2 = 3000$	18/01/2015	OG-590	VPH-Red
VDES J0020-3653	NTT	EFOSC2	$1800 + 1800 = 3600$	25/12/2016	OG530	Gr#16
VDES J0246-5219	NTT	EFOSC2	$2400 + 2400 = 4800$	15/11/2016	OG530	Gr#16
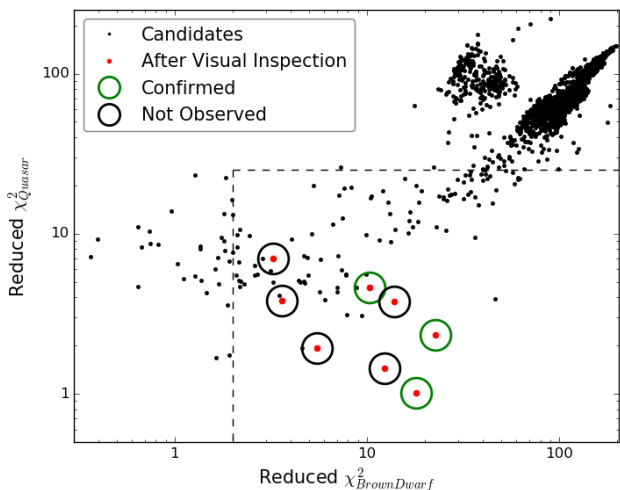
Figure 3. The results of the χ^2 SED fits for the 2360 candidates left after the predicted redshift cuts in Table 1. The dashed lines show the cuts used to narrow down the candidate list for visual inspection. These cuts remove the clearly defined locus of points that have very high χ^2 for both the quasar and brown dwarf model fits. Visual inspection showed these to primarily be objects with contamination in the Y band, such as diffraction spikes. The final eight candidates remaining after visual inspection of all sources in the selection region are shown as the red points. The spectroscopically confirmed quasars are highlighted with green circles.

a custom suite of IDL routines (e.g., Becker et al. 2012). Individual frames were flat-fielded and the sky emission subtracted using an optimal b-spline fit to the sky following Kelson (2003). Relative flux calibration was performed using standard stars. For each detector, a single one-dimensional spectrum was simultaneously extracted from all two-dimensional exposures of a given object using optimal techniques (Horne 1986). Corrections for telluric absorption were done using model transmission curves based on the ESO SKYCALC Cerro Paranal Advanced Sky Model (Noll et al. 2012; Jones et al. 2013). The MagE spectrum can be seen in the third panel of Fig. 5. The optical spectrum and the onset of the Lyα emission line (see R17 for details) imply a redshift of $z = 6.733 \pm 0.008$ for the quasar. Further to the method given in R17 the uncertainties on the redshifts were calculated by taking 100 realisations from the error spectrum and adding them to the spectrum before running them through the same redshift determination method. The uncertainty given is the σ_{MAD} from this distribution.

3.1.2 ESO NTT EFOSC2

The two candidates - VDESJ0246-5219[2] and VDESJ0020-3653 - identified from the DES Y3 data, were observed using the European Southern Observatory's 3.6m New Technology Telescope (NTT). Observations were taken during December 2016 and November 2017 as part of programmes 098.A-0439 and 0100.A-0346 respectively. A summary of the observational setup is given in Table 3. The spectra were reduced using a custom python library designed for reducing high redshift quasar spectra and detailed in R17. Flat fielding and dark subtraction was done using calibration products taken during the afternoon preceding the observations. Cosmic rays were removed from the image using a python implementation (cosmics.py) of the LA cosmics algorithm (van Dokkum 2001). The object was then extracted from the calibrated and cleaned image using a Gaussian extraction kernel and the response function corrected for using standard star measurements. Finally the one-dimensional spectra were flux calibrated to reproduce the observed magnitudes of the object in DES and VHS. The reduced spectra can be seen in the top two panels of Fig. 5 and confirms the identity of both candidates as high-redshift quasars. Based on the onset of the Lyα forest we derive redshifts of 6.90 ± 0.02 and 6.86 ± 0.01 for VDESJ0246-5219 and VDESJ0020-3653 respectively.

3.1.3 Gemini South GMOS

VDESJ0224-4711 was first identified in R17 using DES Y1 data and spectroscopically confirmed as a $z = 6.50$ quasar via observations with the EFOSC2 spectrograph on the European Southern Observatory (ESO)'s New Technology Telescope (NTT). Here we present a new higher spectral resolution, higher S/N rest-frame UV spectrum of the same object taken with the GMOS spectrograph on Gemini-S. Details of the observational setup can be found in Table 3. The data were reduced using the methods outlined in R17 for the Gemini GMOS data and are broadly similar to those employed for the NTT spectral reductions (Section 3.1.2). The new GMOS spectrum for VDESJ0224-4711 can be seen in the bottom panel of Fig. 5.

The new spectrum allows for a better estimate of the quasar ionization near zone size compared to the NTT discovery spectrum. The analysis of near zone sizes for all our high-redshift quasars will be presented in a forthcoming paper. We also derive a new Lyα redshift of $z = 6.514 \pm 0.005$ based on this spectrum (see R17 for details on the redshift estimation method).

---

[2] This quasar was recently independently discovered by Yang et al. (2018)
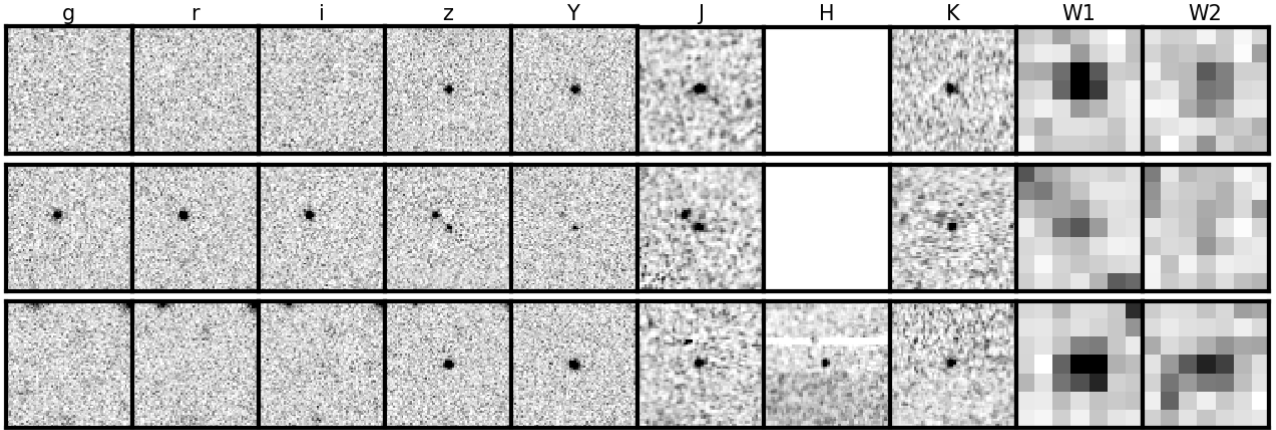
Figure 4. DES optical, VHS near-IR un*WISE* IR 20 arcsecond cutouts of the three new $z > 6.5$ quasars identified in this paper. Top to bottom: VDES J0020-3653, VDES J0246-5219, VDES J0244-5008. All three quasars appear as drop-outs in the DES gri bands as expected. There is no H-band data for the top two objects. In these cutouts North is down and East is to the left.
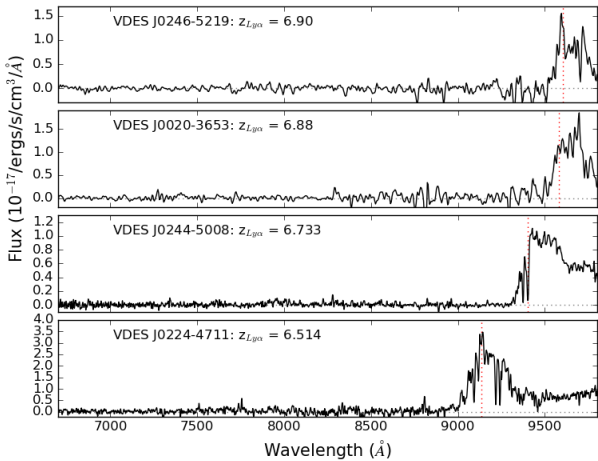
Figure 5. Optical discovery spectra of the three new $z > 6.5$ quasars identified in this work as well as the new Gemini GMOS spectrum of the $z \sim 6.5$ quasar VDESJ0224-4711 (Section 3.1.1) from R17. The red dotted lines mark the derived Lyα redshift for these quasars and the redshifts derived from the onset of the Lyα emission line are indicated in the figure legend.

3.2 Infrared Spectroscopy

3.2.1 Gemini South Flamingos

Near infrared spectra were obtained for VDES J0224-4711 and VDES J0244-5008 using the Flamingos 2 (F2) spectrograph on the Gemini South telescope. We used the long-slit spectroscopy mode with a slit width of 4 pixels (corresponding to 0.72 arcsecs). F2 uses a 2048x2048 Hawaii-II (HgCdTe) detector with 18-micron pixels. There are two grisms used in the setup for these observations, the JH and HK grisms. The JH grism covers 0.9 to 1.8 microns and the HK grism covers 1.2 to 2.4 microns. These can then be combined to give coverage from 0.9 to 2.4 microns in the observed frame.

VDES J0224-4711 was observed on November 2016 and VDES J0244-5008 was observed on January 2017. Both objects were observed for 8×200 second exposures in both JH and HK. The observations were taken in pairs using an ABBA nodding pattern. Each pair was then reduced together: one observation was subtracted from the other to remove artifacts and as a first pass at sky subtraction. The subtracted image was then flat fielded to leave a relatively clean image with a positive and negative trace visible. Each trace was extracted separately and later combined. Wavelength calibration was performed using Argon lines from arc lamp spectra taken during the night of the observations. A 5th order Chebyshev polynomial fit was used to determine the wavelength solution. After the wavelength calibration the median of the eight individual exposures was used as the final output spectrum.

The system response was calculated using observations of the A0V type standard star HIP6364, taken just preceding the observations of the target. The standard star observations were reduced in the same way as the target data with the only difference being that two pairs of observations were taken rather than four. The output spectrum of the star was then divided by an A0V spectral template[3] in order to give the telluric and instrument response correction. Both the near infrared spectra can be seen in the bottom two panels of Fig. 6.

3.2.2 VLT XShooter

VDES J0020-3653 was observed with the XShooter spectrograph on the ESO Very Large Telescope sited at Paranal Observatory in October 2017. The observations were reduced using a custom set of IDL routines (López et al. 2016). The data reduction steps are broadly similar to those described in Section 3.1.1 We did not nod-subtract the X-Shooter NIR frames. Instead, a high S/N composite dark frame was subtracted from each exposure to mitigate the effects of dark current, hot pixels, and other artifacts prior to fitting the sky. The sky model used is again described in Section 3.1.1. The final XShooter near infrared spectrum can be seen in the top panel of Fig. 6.

---

[3] http://axe.stsci.edu/html/templates.html
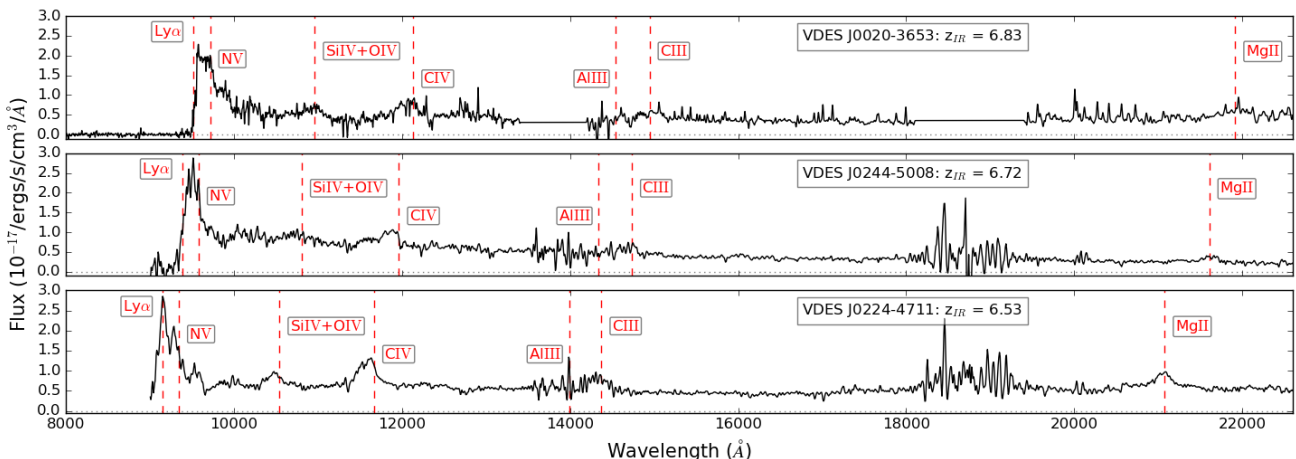
Figure 6. Near infrared spectra of three of our four z>6.5 quasars. The red lines show the positions of spectral lines in the observed frame assuming the MgII derived systemic redshifts from Table 7. The areas of very noisy (or blanked) flux, around 13800Å and 19000Åhave very little flux due to the limited transmission at those wavelengths.

4 EMISSION LINE PROPERTIES

We now consider the emission line properties derived from our near infrared spectra in order to constrain the systemic redshifts, black-hole masses and broad-line region outflow velocities of our high-redshift quasars. The emission lines detected in the near infra-red spectra are generally of modest S/N at the native spectral resolution of these observations. For the purposes of measuring broad emission line properties, high spectral resolution is not a pre-requisite. We therefore create inverse-variance weighted binned spectra of our quasars before spectral fitting.

Line properties are derived from the binned spectra by fitting Gaussian profiles to the broad emission lines after subtraction of a pseudo-continuum, which is made up of a power-law component to model emission from the quasar accretion disk and an FeII template from Vestergaard & Wilkes (2001). Given the modest S/N in the continuum, an FeII template results in an improved fit to the MgII line only for the lowest redshift quasar, VDESJ0224-4711. In order to model the emission line, we begin by fitting a single Gaussian to the line profile and add additional Gaussians only if they are strongly evidenced by the data and result in an improvement in the reduced χ^2 of the fit by >10 per cent.

Uncertainties on the line properties are calculated by generating 100 realisations of the spectra with the flux at each wavelength drawn from a normal distribution with a mean value taken from the best-fit Gaussian model and a standard deviation given by the noise spectrum. The line-fitting is then run on each of these 100 synthetic spectra and the standard deviation of the resulting line-fit parameters are quoted as our formal uncertainties.

4.1 Systemic Redshifts

Robust measures of quasar ionization near zone sizes rely on an accurate estimate of the quasar systemic redshift. It is well known that redshift estimates based on the Lyα emission line can have large systematic offsets as this resonant line is affected by absorption and the kinematics therefore strongly depend on the geometry and distribution of the obscuring material, which affect the scattering of Lyα photons. Redshift estimates based on low-ionization

rest-frame optical emission lines such as MgII, 2798Å on the other hand are generally considered more robust (Hewett & Wild 2010; Shen et al. 2016). Here we make use of our new near infrared spectra to derive systemic redshifts based on MgII and compare them to the Lyα redshifts presented in Section 3.1.

The Gaussian fits to the continuum subtracted MgII line profiles for all 3 quasars can be seen in Fig. 7. While a single Gaussian provides a reasonable fit to VDESJ0244-5008 and VDESJ0020-3653, in the case of VDESJ0224-5711 we find that 2 Gaussians constrained to have the same centroid are necessary in order to adequately fit the broad wings seen in the emission line profile of this object. There is no evidence for a velocity offset between the two Gaussian components in this quasar and we therefore do not allow the centroid of the second Gaussian to be an additional parameter in the fit.

From these Gaussian fits we infer MgII redshifts of 6.526±0.003, 6.724±0.002 and 6.834±0.004 for VDESJ0224-4711, VDESJ0244-5008 and VDESJ0020-3653 respectively. For VDESJ0244-5008, the redshift estimate is consistent with that based on the onset of Lyα but for the other two quasars, Lyα is redshifted by $\delta z \sim 0.01 - 0.03$ relative to MgII.

4.2 Bolometric Luminosities, Black Hole Masses & Eddington Ratios

We calculated bolometric luminosities for our quasars from the rest-frame 3000Å luminosities assuming a bolometric correction of 5.15 (De Rosa et al. 2011). The rest-frame 3000Å luminosities have been calculated by fitting our quasar SED models (Section 2.4) to the available photometry for each quasar and fixing the redshift of the model to the spectroscopic redshift of the quasar estimated from the MgII line. Both values are quoted in Table 4 and the errors are estimated by propagating the errors on the measured photometry.

Black hole masses were calculated from the full-width-half-maximum (FWHM) of the MgII line and using the calibration in Vestergaard & Osmer (2009):
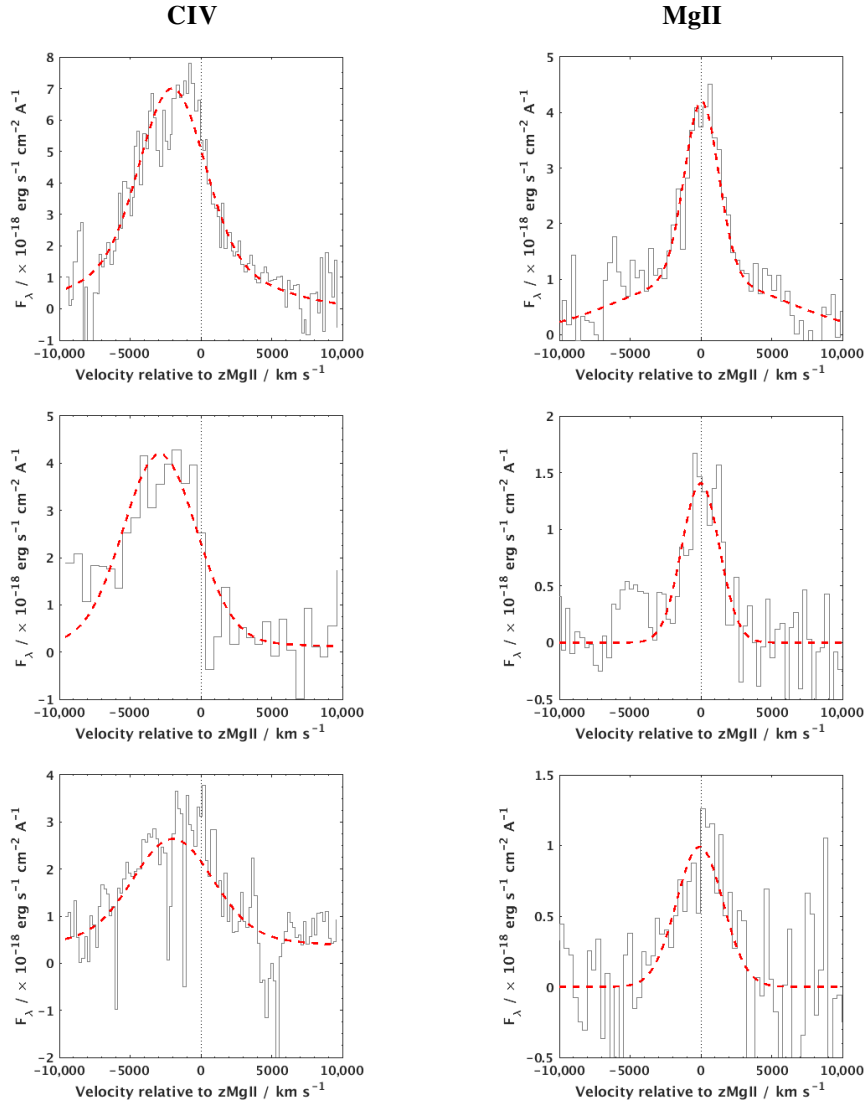
Figure 7. Gaussian fits to the CIV (left) and MgII (right) emission line profiles for VDESJ0224-4711 (top), VDESJ0244-5008 (middle) and VDESJ0020-3653 (bottom). Zero velocity is defined as the MgII peak redshift and shown by the dotted vertical lines.

$$\frac{M_{\mathrm{BH}}}{M_{\odot}} = 10^{6.86} \left(\frac{\mathrm{FWHM_{MgII}}}{1000\mathrm{kms}^{-1}}\right)^2 \left(\frac{L_{3000}}{10^{44}\mathrm{ergs}^{-1}}\right)^{0.5} \quad (1)$$

We derived the FWHM of the MgII from the best-fit Gaussian model and subtracted the instrumental resolution in quadrature from this value. Uncertainties were calculated using the 100 realisations of the line profile with noise added. The FWHM of the MgII line together with the derived black-hole masses are given in Table 4. All three quasars have black-hole masses of $\simeq$1-2$\times10^9 \mathrm{M}_\odot$. The typical systematic uncertainties on these black-hole mass estimates are $\sim$0.3 dex (Shen et al. 2018). Combining with their bolometric luminosities of $\simeq 1-3\times10^{47}$ erg s^{-1} we infer Eddington ratios of close to or just above unity for all three quasars consistent with them being seen during a high-accretion growth phase. In Fig. 8 we compare the bolometric luminosities and black-hole masses to other $z > 6$ quasars from the literature where such observations have been made (De Rosa et al. 2011, 2014; Mazzucchelli et al. 2017; Bañados et al. 2018). Our three new quasars have bolomet-

ric luminosities, black-hole masses and Eddington ratios that are broadly consistent with other high-redshift quasars.

4.3 CIV Blueshifts

The CIV 1550Å emission line in luminous quasars has long been known to display systematic velocity offsets of several thousand km/s blue-ward of systemic (Richards et al. 2002; Baskin & Laor 2005) which are widely thought to be indicative of outflowing gas in the quasar broad-line region (Konigl & Kartje 1994; Murray et al. 1995). Attention has been drawn to the large CIV blueshifts seen in the spectra of the highest redshift quasars (De Rosa et al. 2011; Mazzucchelli et al. 2017), which could indicate that strong disk winds are particularly prevalent in these systems. Changes in the CIV emission line properties of quasars - i.e. blueshift and equivalent width - are themselves correlated with the velocity widths and strengths of other optical and UV emission lines as well as the bolometric luminosity of the quasar (Richards et al. 2011). Recently Coatman et al. (2016) demonstrated that $z \sim 2$ quasars with high CIV blueshifts also exhibit high Eddington ratios. It is

Table 4. Emission line properties of our three $z > 6.5$ quasars with near infra-red spectroscopy.

	VDES J0020-3653	VDES J0244-5008	VDES J0224-4711
Lyα Redshift	6.86 ± 0.01	6.733 ± 0.008	6.514 ± 0.005
MgII Redshift	6.834 ± 0.0004	6.724 ± 0.0008	6.526 ± 0.0003
FWHM$_{\mathrm{MgII}}$ / kms^{-1}	3800 ± 360	3100 ± 530	3500 ± 310 kms
$\lambda\mathrm{L}_\lambda(3000)$ / ergs^{-1}	$(2.62\pm0.05)\times10^{46}$	$(2.79\pm0.05)\times10^{46}$	$(6.08\pm0.09)\times10^{46}$
M$_{\mathrm{BH}}$ / M$_\odot$	$(1.67\pm0.32)\times10^9$	$(1.15\pm0.39)\times10^9$	$(2.12\pm0.42)\times10^9$
L$_{\mathrm{bol}}$ / ergs^{-1}	$(1.35\pm0.03)\times10^{47}$	$(1.44\pm0.02)\times10^{47}$	$(3.13\pm0.04)\times10^{47}$
L$_{\mathrm{bol}}$/L$_{\mathrm{Edd}}$	0.62 ± 0.12	0.96 ± 0.33	1.13 ± 0.22
CIV Blueshift	1700 ± 100 km^{-1}	3200 ± 310 kms^{-1}	2000 ± 160 kms^{-1}
CIV EW (Restframe)	55 ± 1 Å	24 ± 2 Å	44 ± 2 Å
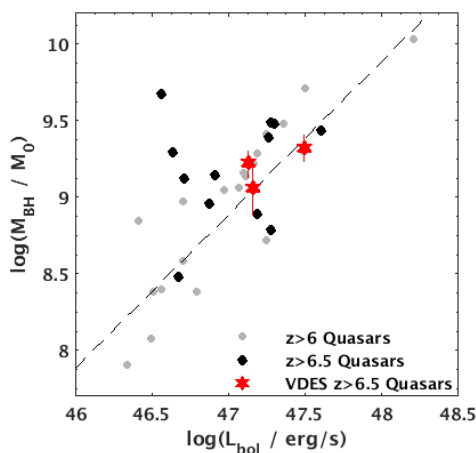
Figure 8. Bolometric luminosity versus black-hole mass for the three $z > 6.5$ quasars in this paper (red symbols). These are compared to $z > 6$ and $z > 6.5$ quasars from the literature (De Rosa et al. 2011, 2014; Mazzucchelli et al. 2017). The dashed line denotes an Eddington ratio of 1.

et al. 2011), where the low-redshift CIV blueshifts have been calculated in an analogous way to the $z > 6.5$ quasars - see Section 3.2 of Coatman et al. (2016). Specifically, the CIV emission line properties for the SDSS quasars were derived using systemic redshift estimates using an Independent Component Analysis (ICA) technique from Allen & Hewett (in preparation), which do not themselves include the CIV line in the systemic redshift estimate - see Coatman et al. (2016, 2017) for a detailed discussion on this issue. The ICA redshifts are completely consistent with the MgII redshifts for SDSS quasars, as well as for our high-redshift sample. However, using the ICA redshifts does allow us to expand the SDSS comparison sample to $z > 2.2$, where MgII is no longer present in the SDSS spectrum. Thus our SDSS low-redshift comparison sample is much larger than those used in previous works e.g. Mazzucchelli et al. (2017). We also note that unlike some other works in the literature we make use of the CIV velocity centroid rather than the peak velocity for all blueshift measurements. As the CIV emission line can have significant flux in the wings of the line, the centroid measure generally results in larger blueshifts compared to the peak.

therefore interesting to explore the CIV emission line properties of our quasars in the context of these previous observations.

We fit the CIV emission lines in our three high-redshift quasars after subtracting a power-law continuum from the spectrum. FeII emission is less strong in this region compared to the MgII region of the spectrum and given the typical S/N of these spectra, we did not consider it necessary to include an FeII component in the continuum. Each component of the CIV doublet is modeled as the sum of two Gaussians with a fixed velocity separation between the doublet components of 390 km/s. The use of two Gaussians to model each component of the doublet allows us to adequately reproduce the asymmetric CIV line profiles, given the typical S/N of our spectra. The CIV blueshifts are derived from the velocity centroid of the CIV emission line relative to the MgII derived systemic redshifts presented in Section 4.1. These blueshifts range from 1700 km/s in VDESJ0020-3653 to 3200 km/s in VDESJ0244-5008 (Table 4). The CIV equivalent widths are also summarised in Table 4. We also calculated CIV line properties in an analogous way for the $z = 6.82$ quasar VHSJ0411−0907 recently discovered by Pons et al. (2018) deriving a blueshift of 830±20 km/s and a rest-frame equivalent width of 32±1Å for this quasar.

In Fig. 9 we compare the CIV blueshifts in our high-redshift sample with a sample of low-redshift quasars from SDSS (Shen

As a result of these updates, a much larger fraction of the low-z SDSS quasars now display significant CIV blueshifts that are comparable to the high-redshift population. Our $z > 6.5$ quasars (as well as those studied e.g. by Mazzucchelli et al. 2017) are also among the highest luminosity, highest Eddington ratio quasars compared to the SDSS population and therefore expected to have large CIV blueshifts compared to the average SDSS quasar. If we select SDSS quasars with $\log_{10}(\mathrm{L}_{\mathrm{bol}}/\mathrm{ergs}^{-1}) > 47.0$ only and compare them to the blueshifts and equivalent widths of our four $z > 6.5$ quasars we find that a two-dimensional Kolmogorov-Smirnov test is consistent with the low and high-redshift quasar populations being drawn from the same continuous distribution. Very recently Shen et al. (2018) reached the same conclusion by comparing the CIV emission line properties of a large sample of $5.7 \lesssim z \lesssim 6.4$ quasars to lower redshift quasars from SDSS. We have deliberately not included the Mazzucchelli et al. (2017) quasars in our test as we cannot confirm that the same line-fitting prescriptions have been used to calculate CIV emission line properties for these quasars as we have done here both for the high-redshift and low-redshift SDSS quasars. At face-value however there are three quasars in Mazzucchelli et al. (2017) with very large blueshifts of >4000 km/s, which would seem inconsistent with being drawn from the same distribution as the low redshift SDSS quasars.
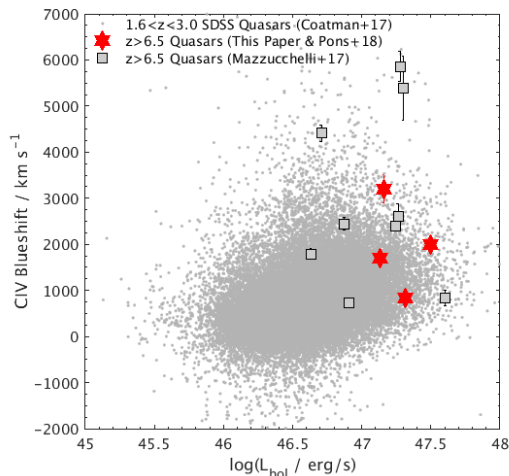
Figure 9. CIV blueshift versus quasar luminosity for the three $z > 6.5$ quasars in this paper and the $z = 6.82$ quasar from Pons et al. (2018) (red symbols). These are compared to low-redshift quasars from SDSS as well as the $z > 6.5$ quasars studied in Mazzucchelli et al. (2017).

5 DISCUSSION AND CONCLUSIONS

We have described the discovery of three new quasars at $6.7 \lesssim z \lesssim 6.9$ identified using imaging data from the Dark Energy Survey Year 3 data release, VISTA Hemisphere Survey and *WISE*. These discoveries show that our SED-fitting method to identify $z \sim 6$ quasars from wide-field imaging surveys (R17) can easily be adapted to produce clean, low-contamination samples at even higher redshifts of $z > 6.5$. The three new quasars have $J_{AB} = 20.2$ to 21.3 ($M_{1450} = -25.6$ to -26.6) and span the full luminosity range covered by other quasar samples at these high redshifts. They are at redshifts of 6.724, 6.834 and 6.90.

We obtained near infra-red spectra for three of the four $z \geqslant 6.5$ quasars identified by us using DES+VHS, to constrain their black-hole masses, Eddington ratios and CIV blueshifts. The systemic redshifts derived from the MgII emission lines in these near infrared spectra are 6.526, 6.724 and 6.834. In two out of the three quasars the Lyα emission line is redshifted by $\delta z \sim 0.01$-0.03 relative to MgII. Our new quasars have black-hole masses of $\simeq 1$ - $2 \times 10^9 M_\odot$ and are accreting close to or above the Eddington limit, with derived Eddington ratios of ~ 0.6-1.1 in the sample. This is broadly consistent with what is found for other quasars at these highest redshifts (Mazzucchelli et al. 2017; Bañados et al. 2018).

Several of our $z > 6.5$ quasars exhibit large CIV blueshifts of several thousand km/s. We have demonstrated however that if we compare the sample to lower redshift SDSS quasars of similar luminosity and where the CIV blueshift is measured in an analogous way to the high-redshift population, the distribution of CIV blueshifts and equivalent widths in our $z > 6.5$ sample is completely consistent with the low-redshift population. Therefore it appears that high-mass, high accretion rate quasars have very similar broad-line region outflow properties regardless of the epoch at which they are observed.

Overall our new quasars now add to the growing census of high-luminosity, highly-accreting supermassive black holes seen well into the Epoch of Reionisation. Based on extrapolations of the $z \sim 6$ luminosity functions from Willott et al. (2010) and Jiang et al. (2016) we expect to find ~ 15-20 quasars at $6.5 < z < 7.2$

down to a DES Y-band flux limit of <21.0 and over the full DES survey area of 5000 sq-deg. Thus the four new quasars identified in this paper are expected to form only a small subset of the $z > 6.5$ quasars that will be identified using the final DES+VHS data releases.

This analysis makes use of the cosmics.py algorithum based on the L.A. Cosmic algorithm detailed in van Dokkum (2001).

REFERENCES

Abbott T. M. C., et al., 2018, preprint, p. arXiv:1801.03181 (arXiv:1801.03181)
Bañados E., et al., 2016, ApJS, 227, 11
Bañados E., et al., 2018, Nature, 553, 473
Banerji M., et al., 2015, MNRAS, 446, 2523
Baskin A., Laor A., 2005, MNRAS, 356, 1029
Becker G. D., Sargent W. L. W., Rauch M., Carswell R. F., 2012, ApJ, 744, 91
Bolton J. S., Haehnelt M. G., 2007, MNRAS, 374, 493
Coatman L., Hewett P. C., Banerji M., Richards G. T., 2016, MNRAS, 461, 647
Coatman L., Hewett P. C., Banerji M., Richards G. T., Hennawi J. F., Prochaska J. X., 2017, MNRAS, 465, 2120
De Rosa G., Decarli R., Walter F., Fan X., Jiang L., Kurk J., Pasquali A., Rix H. W., 2011, ApJ, 739, 56
De Rosa G., et al., 2014, ApJ, 790, 145
Fan X., Carilli C. L., Keating B., 2006, ARA&A, 44, 415
Hewett P. C., Wild V., 2010, MNRAS, 405, 2302
Horne K., 1986, PASP, 98, 609
Jiang L., et al., 2016, preprint, (arXiv:1610.05369)
Jones A., Noll S., Kausch W., Szyszka C., Kimeswenger S., 2013, A&A, 560, A91
Kelson D. D., 2003, PASP, 115, 688
Kirkpatrick J. D., Cushing M. C., Gelino C. R., Griffith R. L., Skyrutskie M. F., Marsh K. A., Wright E. L., Mainzer A., 2011, ApJS, 197, 19
Konigl A., Kartje J. F., 1994, ApJ, 434, 446
Latif M. A., Schleicher D. R. G., Schmidt W., Niemeyer J., 2013, MNRAS, 433, 1607
López S., et al., 2016, A&A, 594, A91
Maddox N., Hewett P. C., 2006, MNRAS, 367, 717
Maddox N., Hewett P. C., Péroux C., Nestor D. B., Williamssotzki L., 2012, MNRAS, 424, 2876
Matsuoka Y., et al., 2018a, PASJ, 70, S35
Matsuoka Y., et al., 2018b, ApJS, 237, 5
Mazzucchelli C., et al., 2017, ApJ, 849, 91
McMahon R. G., Banerji M., Gonzalez E., Koposov S. E., Bejar B. V. J., Lodieu N., Rebolo R., VHS Collaboration 2013, The Messenger, 154, 35
Meisner A. M., Lang D., Schlegel D. J., 2017, AJ, 154, 161
Mortlock D. J., et al., 2011, Nature, 474, 616
Murray N., Chiang J., Grossman S. A., Voit G. M., 1995, ApJ, 451, 498
Noll S., Kausch W., Barden M., Jones A. M., Szyszka C., Kimeswenger S., Vinther J., 2012, A&A, 543, A92
Pons E., McMahon R. G., Simcoe R. A., Banerji M., Hewett P. C., Reed S. L., 2018, arXiv e-prints, p. arXiv:1812.02481
Reed S. L., et al., 2017, MNRAS, 468, 4702
Richards G. T., Fan X., Newberg H. J., Strauss M. A., Vanden Berk D. E., Schneider D. P., Yanny B., 2002, The Astronomical Journal, 123, 2945
Richards G. T., et al., 2011, AJ, 141, 167
Shen Y., et al., 2011, ApJS, 194, 45
Shen Y., et al., 2016, ApJ, 831, 7
Shen Y., et al., 2018, preprint, (arXiv:1809.05584)
Sijacki D., Springel V., Haehnelt M. G., 2009, MNRAS, 400, 100
Skrzypek N., Warren S. J., Faherty J. K., Modesrtlock D. J., Burgasser A. J., Hewett P. C., 2015, A&A, 574, A78
Venemans B. P., Findlay J. R., Sutherland W. J., De Rosa G., McMahon R. G., Simcoe R., González-Solares E. A., et al., 2013, ApJ, 779, 24
Venemans B. P., et al., 2015a, MNRAS, 453, 2259
Venemans B. P., et al., 2015b, ApJ, 801, L11
Vestergaard M., Osmer P. S., 2009, ApJ, 699, 800
Vestergaard M., Wilkes B. J., 2001, ApJS, 134, 1
Volonteri M., 2010, A&A Rev., 18, 279

Wang F., et al., 2017, ApJ, 839, 27
Wang F., et al., 2018, preprint, (arXiv:1810.11926)
Willott C. J., et al., 2010, The Astronomical Journal, 139, 906
Wright E. L., et al., 2010, ApJ, 140, 1868
Yang J., et al., 2018, preprint, (arXiv:1811.11915)
van Dokkum P. G., 2001, PASP, 113, 1420

AFFILIATIONS

[1]Department of Astrophysical Sciences, 4 Ivy Lane, Princeton University, Princeton, NJ 08544
[2]Institute of Astronomy, University of Cambridge, Madingley Road, Cambridge CB3 0HA, UK
[3]Kavli Institute for Cosmology, University of Cambridge, Madingley Road, Cambridge CB3 0HA, UK
[4]Department of Physics and Astronomy, University of California, 900 University Avenue, Riverside, CA 92521, USA
[5]Center for Cosmology and Astro-Particle Physics, The Ohio State University, Columbus, OH 43210, USA
[6]Department of Astronomy, The Ohio State University, Columbus, OH 43210, USA
[7]Observatories of the Carnegie Institution for Science, 813 Santa Barbara Street, Pasadena, CA 91101, USA
[8]Cerro Tololo Inter-American Observatory, National Optical Astronomy Observatory, Casilla 603, La Serena, Chile
[9]Fermi National Accelerator Laboratory, P. O. Box 500, Batavia, IL 60510, USA
[10]Institute of Cosmology and Gravitation, University of Portsmouth, Portsmouth, PO1 3FX, UK
[11]CNRS, UMR 7095, Institut d'Astrophysique de Paris, F-75014, Paris, France
[12]Sorbonne Universités, UPMC Univ Paris 06, UMR 7095, Institut d'Astrophysique de Paris, F-75014, Paris, France
[13]Department of Physics & Astronomy, University College London, Gower Street, London, WC1E 6BT, UK
[14]Centro de Investigaciones Energéticas, Medioambientales y Tecnológicas (CIEMAT), Madrid, Spain
[15]Laboratório Interinstitucional de e-Astronomia - LIneA, Rua Gal. José Cristino 77, Rio de Janeiro, RJ - 20921-400, Brazil
[16]Department of Astronomy, University of Illinois at Urbana-Champaign, 1002 W. Green Street, Urbana, IL 61801, USA
[17]National Center for Supercomputing Applications, 1205 West Clark St., Urbana, IL 61801, USA
[18]Institut de Física d'Altes Energies (IFAE), The Barcelona Institute of Science and Technology, Campus UAB, 08193 Bellaterra (Barcelona) Spain
[19]Institut d'Estudis Espacials de Catalunya (IEEC), 08034 Barcelona, Spain
[20]Institute of Space Sciences (ICE, CSIC), Campus UAB, Carrer de Can Magrans, s/n, 08193 Barcelona, Spain
[21]Kavli Institute for Particle Astrophysics & Cosmology, P. O. Box 2450, Stanford University, Stanford, CA 94305, USA
[22]Department of Physics and Astronomy, University of Pennsylvania, Philadelphia, PA 19104, USA
[23]Observatório Nacional, Rua Gal. José Cristino 77, Rio de Janeiro, RJ - 20921-400, Brazil
[24]Department of Physics, IIT Hyderabad, Kandi, Telangana 502285, India
[25]Department of Astronomy, University of Michigan, Ann Arbor, MI 48109, USA
[26]Department of Physics, University of Michigan, Ann Arbor, MI 48109, USA
[27]Kavli Institute for Cosmological Physics, University of Chicago, Chicago, IL 60637, USA
[28]Instituto de Fisica Teorica UAM/CSIC, Universidad Autonoma de Madrid, 28049 Madrid, Spain
[29]Department of Physics, Stanford University, 382 Via Pueblo Mall, Stanford, CA 94305, USA

[30]SLAC National Accelerator Laboratory, Menlo Park, CA 94025, USA

[31]Santa Cruz Institute for Particle Physics, Santa Cruz, CA 95064, USA

[32]Department of Physics, The Ohio State University, Columbus, OH 43210, USA

[33]Max Planck Institute for Extraterrestrial Physics, Giessenbachstrasse, 85748 Garching, Germany

[34]Universitäts-Sternwarte, Fakultät für Physik, Ludwig-Maximilians Universität München, Scheinerstr. 1, 81679 München, Germany

[35]Harvard-Smithsonian Center for Astrophysics, Cambridge, MA 02138, USA

[36]Australian Astronomical Optics, Macquarie University, North Ryde, NSW 2113, Australia

[37]Departamento de Física Matemática, Instituto de Física, Universidade de São Paulo, CP 66318, São Paulo, SP, 05314-970, Brazil

[38]George P. and Cynthia Woods Mitchell Institute for Fundamental Physics and Astronomy, and Department of Physics and Astronomy, Texas A&M University, College Station, TX 77843, USA

[39]Institució Catalana de Recerca i Estudis Avançats, E-08010 Barcelona, Spain

[40]Jet Propulsion Laboratory, California Institute of Technology, 4800 Oak Grove Dr., Pasadena, CA 91109, USA

[41]School of Physics and Astronomy, University of Southampton, Southampton, SO17 1BJ, UK

[42]Instituto de Física Gleb Wataghin, Universidade Estadual de Campinas, 13083-859, Campinas, SP, Brazil

[43]Computer Science and Mathematics Division, Oak Ridge National Laboratory, Oak Ridge, TN 37831

[44]Argonne National Laboratory, 9700 South Cass Avenue, Lemont, IL 60439, USA